X-ray resonant magnetic scattering study of the magnetic coupling in Co/Pt nanolines and its evolution under magnetic field

K. Chesnel,[1,*] M. Belakhovsky,[1,†] S. Landis,[2] J. C. Toussaint,[3] S. P. Collins,[4] G. van der Laan,[4] E. Dudzik,[5] and S. S. Dhesi[6]

[1]*CEA Grenoble, Département de Recherche Fondamentale sur la Matière Condensée, Service de Physique des Matériaux et Microstructures, 17, Rue des Martyrs, F-38054 Grenoble Cedex 9, France*

[2]*CEA Grenoble, DTS/STME/LLG, 17 avenue des Martyrs, 38054 Grenoble, France*

[3]*Laboratoire Louis Néel, CNRS, BP 166, 38042, Grenoble Cedex 09, France*

[4]*Magnetic Spectroscopy Group, Daresbury Laboratory, Warrington WA4 4AD, United Kingdom*

[5]*Hahn-Meitner-Institut, Glienicker Str. 100, D-14109 Berlin, Germany*

[6]*ESRF, BP 220, 38043 Grenoble, France*

(Received 11 September 2001; revised manuscript received 18 January 2002; published 26 July 2002)

Periodic arrays of silicon nanolines, covered by a Co/Pt multilayer, with perpendicular magnetization, have been studied by soft x-ray resonant magnetic scattering at the Co L_3 edge. At the resonance, magnetic signals appear both on top of the structural diffraction peaks, characteristic of the grating, and between these peaks. These superstructure satellites reveal an antiferromagnetic order, generated by the interline dipolar coupling. Their intensities are strongly sensitive to the magnetic history, and can be enhanced through specific demagnetization processes. By applying an *in situ* magnetic field, the evolution of the magnetic signal has been monitored through the entire hysteresis loop. The magnetic contribution of the structural superlattice peaks can be quantified by their asymmetry ratio, whose angular variation stems from the scattering factor. The change of the purely magnetic satellites with the magnetic field is completely reproducible and characterizes the modifications of the magnetic configuration during the reversal process. A model of Ising macrospins, from which the distribution of the magnetic reversal fields can be deduced, is shown to be in agreement with the measured results.

DOI: 10.1103/PhysRevB.66.024435 PACS number(s): 75.70.−i, 75.75.+a, 75.60.−d

I. INTRODUCTION

Submicron magnetic structures have become increasingly attractive systems for future applications in ultrahigh density storage.[1] It is therefore important to understand the magnetic correlation between these small objects and their evolution in an external magnetic field, in order to be able to manipulate the magnetic distribution of the whole pattern through individual reversal processes. In this work, we focus on arrays of magnetic lines with perpendicular magnetization obtained by depositing Co/Pt on an etched silicon pattern. The aim of this study is to describe the magnetic order in the one-dimensional (1D) grating, as a first step before going to the 2D pattern of magnetic dots.

The present study uses the technique of x-ray resonant magnetic scattering (XRMS), which is based on the resonance effect in the light-matter magnetic interaction,[2–4] and can be considered as an x-ray analog of the optical Kerr effect. This technique is classically used in the hard x-ray limit in order to access to the magnetization on the atomic scale;[5] in our case the measurement is performed in the soft x-ray range, and allows us to evidence the magnetic order at the submicron length scale. The photon energy is tuned to the L_3 absorption edge of the magnetic element (e.g., Co), in order to promote the dipole transition from the spin-orbit split p state into the magnetic $3d$ valence band. The wavelength at the Co L_3 edge (1.59 nm) is well matched to study the magnetic correlation of a nanometric grating. Complementary to magnetic force microscopy (MFM), this technique has the specific advantage of being sensitive to the three-dimensional magnetization profile and its evolution under applied magnetic field. Furthermore, its element specificity is beneficial to the study of heterogeneous systems.

II. SAMPLE DESCRIPTION

The nanoline gratings are fabricated by a special technique. The conventional method to prepare such systems is to etch the sample *after* the deposition of the magnetic film.[6] In our case, the magnetic material, a Co/Pt multilayer, is deposited onto a pre-etched Si substrate obtained by reactive ion etching at the Silicon Department of Technology (DTF) at the CEA-Grenoble. This technique has the advantages to keep a high etching resolution and to eliminate any deterioration of the magnetic layer during patterning.[7] The different steps involved in the sample preparation are summarized in Fig. 1.

Step 1: deposition of a 600-nm film of negative resist onto the silicon wafer. Step 2: insulation of parallel lines on the resist with a scanning electron beam and development of the insolated resist. Step 3: reactive ion etching to transfer the pattern onto the silicon substrate. Step 4: deposition of a Pt (18 Å)/ $[\text{Co (5 Å)/ Pt (18 Å)}]_{13}$ multilayer by dc sputtering at room temperature, at normal incidence for Co atoms and at oblique incidence for Pt atoms, producing a magnetic 32-nm thin film with perpendicular magnetic anisotropy (PMA).

The Si lines used in the present study are labeled by $(L/d/h)$, where L is the linewidth (from 200 to 400 nm), d is

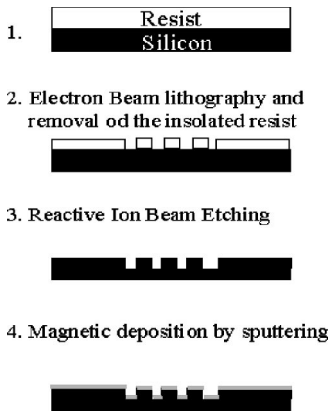

FIG. 1. Patterning process.

the line spacing (75 or 200 nm), and h is the trench height (35 or 300 nm). The etched area for each geometry covers 2×2 mm^2. Figure 2 shows an atomic force microscopy (AFM) image of the silicon array at the end of the patterning process for the (200/200/35) geometry on a 2-μm scale.

In a previous work,[8] we studied the effect of the geometrical parameters on the magnetic interline correlation, and showed that small line separations (d) and deep trenches (h) favor an AF ordering. In this paper, we will concentrate on the (200/75/300) configuration for two main reasons. First, in this deep-trench configuration, the magnetic film covers only the top of the lines, with a limited amount of material along the sidewalls, and practically nothing at the bottom of the trenches. This structural discontinuity leads to a magnetic discontinuity, i.e., there is no exchange interaction linking the tops through the side walls and trenches, so that only dipolar coupling is present between the separated magnetic lines. Second, this dipolar interaction is stronger when the separation between the tops is smaller.

Two complementary techniques were used to study this magnetic system. On the one hand, the MFM technique, sensitive to the magnetic stray fields, provides a surface image of the magnetic domains over a small area (typically 5×5 μm^2). On the other hand, XRMS, on which this work is centered, is sensitive to the volume magnetization and its distribution over a wider area. Indeed, the illuminated area covers 650 μm$\times2$ mm, and at the Co L_3 resonance energy of 778 eV, the attenuation length is about 70 nm, which allows us to probe the entire magnetic layer, at an incidence

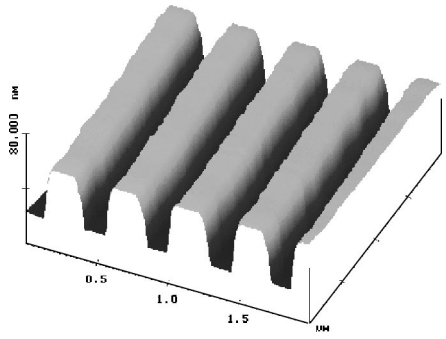

FIG. 2. AFM image of a (200/200/35) line grating.

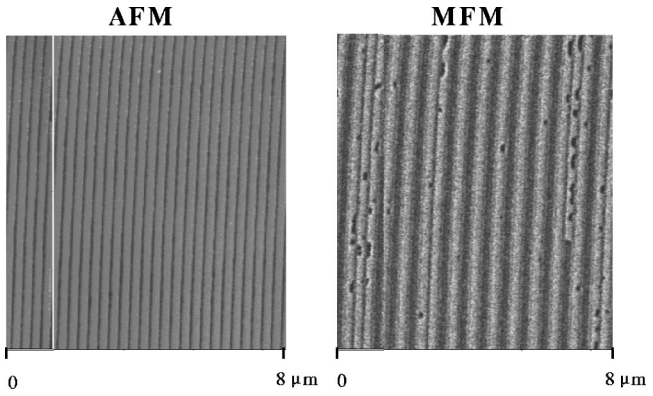

FIG. 3. Comparison of AFM (charge profile, left) and MFM (magnetic profile, right) images of a small area (8×8 μm) for lines grating with the (200/75/300) geometry.

angle of 18°. Neither of the two techniques is sensitive to magnetism in regions other than the tops of the lines: the MFM tip cannot image deep trenches (300 nm here), and the strong absorption of the soft x rays prevents any scattered signal from them. One can therefore safely consider the magnetization on the line tops only. In this context, we can study the lateral line correlations and their evolution under field.

The comparison between the AFM and MFM images, presented in Fig. 3, illustrates the local magnetic order. On the AFM image, the contrast shows the regular topography (line tops are light; trenches dark), whose period is 275 nm. The MFM, obtained after subtracting this topography, shows the pure perpendicular magnetic contours. The magnetic tip is sensitive to the stray field produced by the top of the lines only; light and dark areas correspond to ''up'' and ''down'' magnetizations of these lines. Every line in the image appears mostly as a single domain, but one can find different magnetic arrangements in the line pattern: adjacent lines can have the same darkness, displaying a tendency toward ferromagnetic order (FM) with the same periodicity as the topography, while at other places, light and dark alternation occurs, pointing to co-existing antiferromagnetic (AF) order, whose period is twice that of the structural one.

These magnetic arrangements depend on the magnetic history and change when an external magnetic field is applied. The first approach of the magnetization reversal processes consists in measuring the hysteresis curve. Figure 4 shows a polar Kerr effect measurement with the magnetic field perpendicular to the layer. The coercive field $H_c=780$ Oe in this nanoline pattern is larger than in a continuous Co/Pt multilayer, giving only $H_c=330$ Oe. The increase of the coercive value arises from nanostructuring.[9]

Using the XRMS technique, one can determine the lateral magnetic correlation over a wide area of the line grating. The application of an *in situ* magnetic field allows us to monitor the magnetic evolution of this periodic profile through the whole hysteresis loop, from one saturated state to the opposite saturated state. This provides important information for understanding and quantifying the reversal processes around the coercive points.

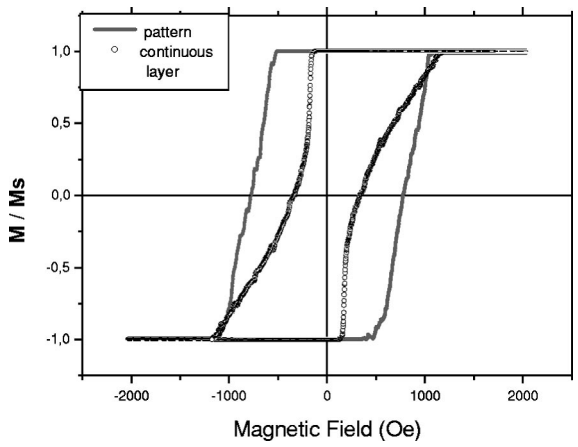

FIG. 4. Kerr effect measurement on a (200/75/300) line magnetic pattern and on a continuous layer using a perpendicular magnetic field.

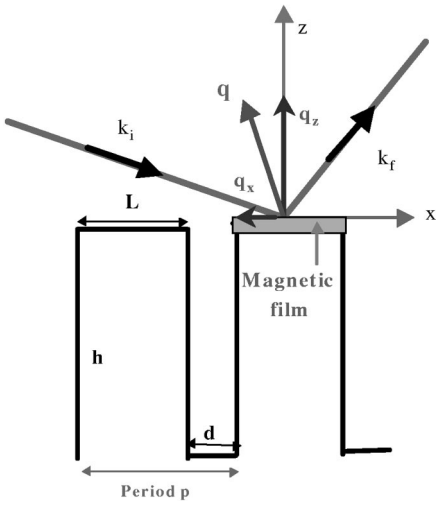

FIG. 5. Diffraction geometry with the sample geometry. The wave vector $\mathbf{q}=\mathbf{k}_f-\mathbf{k}_i$ is split into two components q_z and q_x.

III. XRMS MEASUREMENTS

In the kinematical approximation, the detected intensity is proportional to the square modulus of the scattering form factor, summed over all positions $\mathbf{r}_n$ of the magnetic material,

$$I \propto \left| \sum_n f_n \exp(i\mathbf{q}\cdot\mathbf{r_n}) \right|^2, \tag{3.1}$$

where $\mathbf{q}$ is the scattering vector and f_n the atomic scattering amplitude.

The general expression of the scattering amplitude has been given by Hannon *et al.*,[10] showing that f_n describes both nonmagnetic and magnetic contributions, with the latter enhanced by several decades at an proper resonance energy. We study the resonant magnetic signal, which corresponds to an electric dipole transition ($E1$) between the $2p$ level and the d band of the Co atoms ($L_{2,3}$ edges). The sensitivity to the magnetism in such a process is due to the presence of spin-orbit interaction in the core-hole state ($2p_{1/2}$, $2p_{3/2}$) and exchange interaction in the d band, which act as spin dependent emitter and detector, respectively. In the case of an $E1$ transition, f_n can be written as

$$f_n^{res} = \mathbf{e}_f^* \cdot \mathbf{e}_i F^{(0)} - i(\mathbf{e}_f^* \times \mathbf{e}_i)\cdot \mathbf{M}_n F^{(1)} + (\mathbf{e}_f^* \cdot \mathbf{M}_n)(\mathbf{e}_i \cdot \mathbf{M}_n) F^{(2)}, \tag{3.2}$$

where $\mathbf{e}_f$ and $\mathbf{e}_i$ are the polarization vectors of the incident and the scattered light, respectively, $\mathbf{M}_n$ is the unit vector of the magnetization, and the $F^{(0,1,2)}$ describe the atomic electric-dipole resonance processes,

$$F^{(0)} = F_{1,1} + F_{1,-1},$$

$$F^{(1)} = F_{1,1} - F_{1,-1},$$

$$F^{(2)} = 2F_{1,0} - F_{1,1} - F_{1,-1}. \tag{3.3}$$

The spectroscopic terms account for the transition amplitudes for electric L-pole radiation, with angular momentum component M. These factors are strongly enhanced at the absorption edges due to the resonant denominator, allowing the observation of a strong XRMS signal in addition to the structural scattering.[10]

The scattering amplitude f_n^{res} in Eq. (3.2) is the sum over three terms. The first one, corresponding to the isotropic scattering, is proportional to the electronic charge density and gives the main contribution to the scattered intensity. The other two terms depend on the magnetization unit vector and are weaker. The second term depends linearly on the magnetization, while the third term, even weaker still, has a quadratic dependence, and can give second-order magnetic diffraction peaks. The magnetization direction can lead to a photon polarization change between the σ and π channels. The possible transitions are $\sigma \rightarrow \pi, \pi \rightarrow \sigma$, and $\pi \rightarrow \pi$. Circularly polarized light, containing out-of-phase σ and π components, can lead to interference in the final channel π.[11]

Experiments were performed at beamline ID12B and ID8 of the European Synchrotron Radiation Facility (ESRF) in France. The light, produced by the helical undulator, was circularly polarized (94%). The setup used is a vacuum two-circle diffractometer,[12,13] equipped with an electromagnet fixed onto the sample holder plate providing a perpendicular field up to 0.18 T.

The sample was placed in a transverse geometry, in which the line pattern was perpendicular to the diffraction plane, as shown in Fig. 5. The combination of sample and detector rotations allows scanning of the wave vector $\mathbf{q}$, either along $\mathbf{q}_z$ (perpendicularly to the surface) or along $\mathbf{q}_x$ (in the layer plane and perpendicular to the lines). Any magnetic contribution appearing at a certain value q_{x0} for fixed q_z reveals the periodic nature of the magnetic profile in the x direction. The intensity modulations along magnetic rods (obtained by varying q_z at fixed q_{x0}) reproduce the magnetic depth profile inside the multilayer.[8] In this report, we focus on the variation of the scattered intensity along q_x.

IV. RESULTS AND ANALYSIS

A. Magnetic signal

The aim of the XRMS measurements is to observe the magnetic order in the perpendicularly magnetized line array.

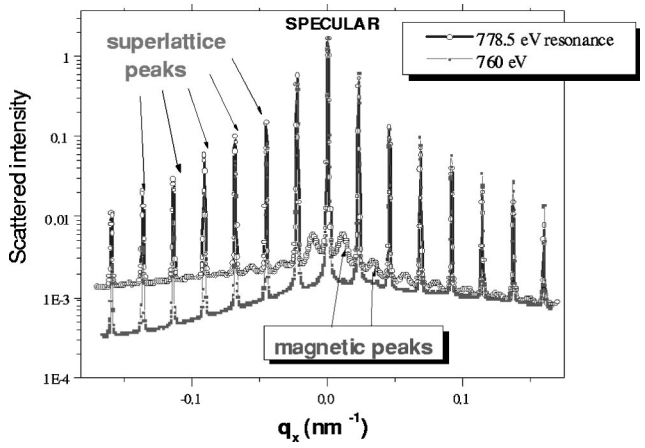

FIG. 6. Normalized diffraction pattern along q_x on the first multilayer Bragg peak ($q_z = 0.24$ Å^{-1}) for two energies: $E = 760$ eV (below the edge) and $E = 778.5$ eV (at resonance).

The possibility to tune the photon energy around the Co L_3 edge enables independent measurements of the structural order (at any energy) and the magnetic order (at the resonance energy). As shown in Fig. 6, the structural diffraction pattern, measured at 760 eV, exhibits many superlattice peaks around the central specular reflection. The peak positions correspond to the structural period $p = 275$ nm and their intensities are modulated by an envelope function, due to the form factor given by the shape of the film deposited on the patterned structure. The asymmetry of the spectrum is due to the asymmetry of the sputtering process (the Pt atoms were deposited at 35° oblique incidence angle). Indeed, this asymmetric shape is reversed when the sample is rotated by 180°.

Near the Co L_3 resonance energy, pure magnetic satellites appear between the structural peaks. The value of this magnetic resonance energy has been chosen in order to maximize the intensity of the magnetic signal, as shown in Fig. 7, and

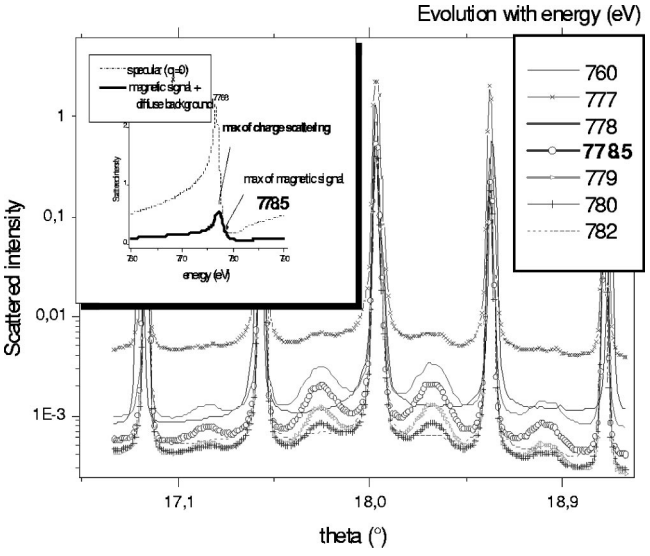

FIG. 7. Evolution of the diffraction pattern with incident photon energy. Inset: intensity variation as a function of photon energy for the specular peak and the first magnetic bump.

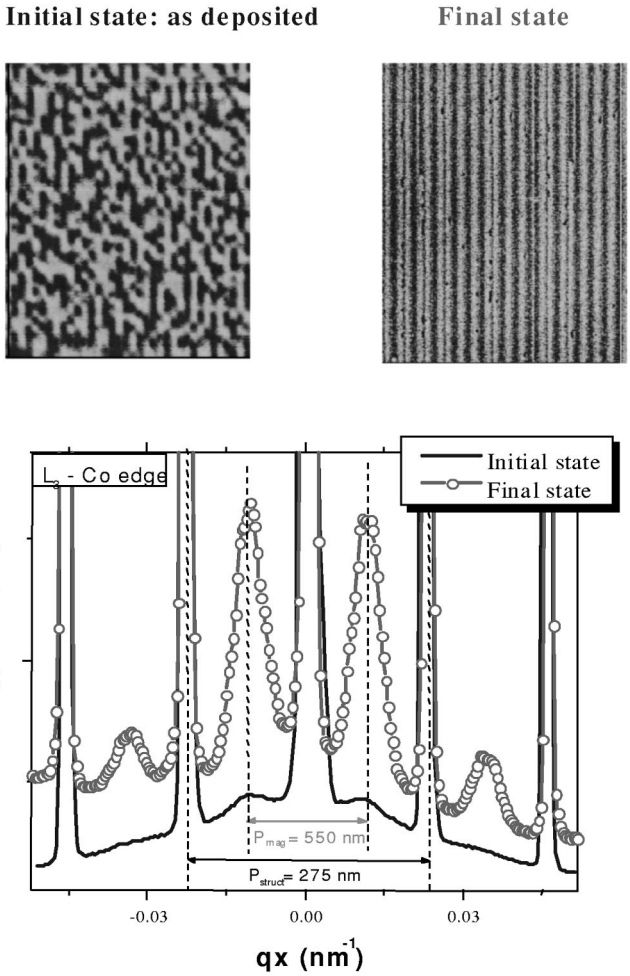

FIG. 8. Influence of a demagnetization process on the XRMS signal for a (200/75/300) sample, at $E = 778.5$ eV. Top: MFM images showing the initial state (left) and the final state (right) after demagnetization.

corresponds to $E = 778.5$ eV. This value is 1.7 eV above the structural resonance. It is clear from Fig. 6 that the position of the satellites ($q_x = 0.011$ nm^{-1} for the first order) corresponds to a magnetic period $p_M = 570$ nm, twice the structural one, thus revealing the presence of antiferromagnetic (AF) ordering of the lines, i.e., up/down alternation. The large width of the satellites, $\Delta q_x = 0.006$ nm^{-1} full width at half maximum (FWHM), indicates that this order has a short correlation length ($l_c = 1000$ nm), which covers only four lines. Indeed, as shown by the MFM images (cf. Fig. 3), the magnetic configuration in such a system contains a mixing of antiferromagnetic (AF) and ferromagnetic (FM) areas. Incidentally, the shape of the spectrum observed by XRMS at the resonance edge is less asymmetric than at 760 eV. Indeed, at the Co-L_3 edge, the attenuation length is strongly reduced and the x rays are not sensitive to the material deposited on the sidewalls, which induces part of the structural asymmetry. Furthermore, since magnetism is present only on the lines top and practically absent in the small amount of material along the sidewalls, the magnetic profile is completely different than the structural one. As we will show, XRMS

gives the possibility to follow rapidly the influence of the magnetic history on the AF tendency or its evolution with an external magnetic field.

B. Influence of magnetic history

We consider here the effect of the magnetic history, specifically of the demagnetization processes on the magnetic peaks. As deposited, the sample exhibits a complicated magnetic configuration, as shown by MFM image (Fig. 8, top left). One can observe a succession of small magnetic domains along each line, while all lines exhibit single domains across their width. In order to favor the magnetic domain growth, the sample was demagnetized by gently decreasing the field (with a speed of 1 Oe/s) from saturation down to the coercive value and then quickly to zero. The MFM image of the resulting magnetic configuration shows that the imaged region of almost every line has become a single domain, strengthening the lateral AF order. As a result, the XRMS spectrum shows much stronger magnetic satellites, up by a factor of 20 for the first order. Such an enhancement can be attributed to two phenomena: first, the increase of the magnetic correlation length along the line's direction reduces the longitudinal scattering and thus concentrates the scattered intensity at $q_y=0$; second, the AF coupling reinforces the scattered intensity in this direction. In order to understand more quantitatively this result, a measure of the magnetic peak intensities as a function of the *in situ* magnetic field was performed.

C. Evolution under field

The possibility to apply a perpendicular magnetic field **B** *in situ* with an electromagnet inside the diffraction chamber enables monitoring of the evolution of the XRMS spectrum with field strength. It is particularly interesting to study the evolution of the magnetic AF satellites and structural peak intensities of different orders when the magnetic field cycles through the whole hysteresis loop, as shown in Fig. 9. The main advantage of these measurements is the possibility to follow the signal in real time, with a good time resolution (about 10 Oe/sec here), compared to MFM studies, which cannot be performed under continuous field variation and which requires more time.

1. At the grating periodicity

The top four plots of Fig. 9 show the intensity variation for the specular peak (a) and the superlattice peaks: left (b) and right (b′) first order, and left (c) and right (c′) second order. In all cases, we observe the magnetic contribution in the scattering process, revealing forms reminiscent of magnetization hysteresis loops. This effect is due to interference between the structural and the magnetic terms in the total scattering factor [see Eq. (3.2)], which can be decomposed into two terms:

$$f_n^{res}=F_S+F_M, \tag{4.1}$$

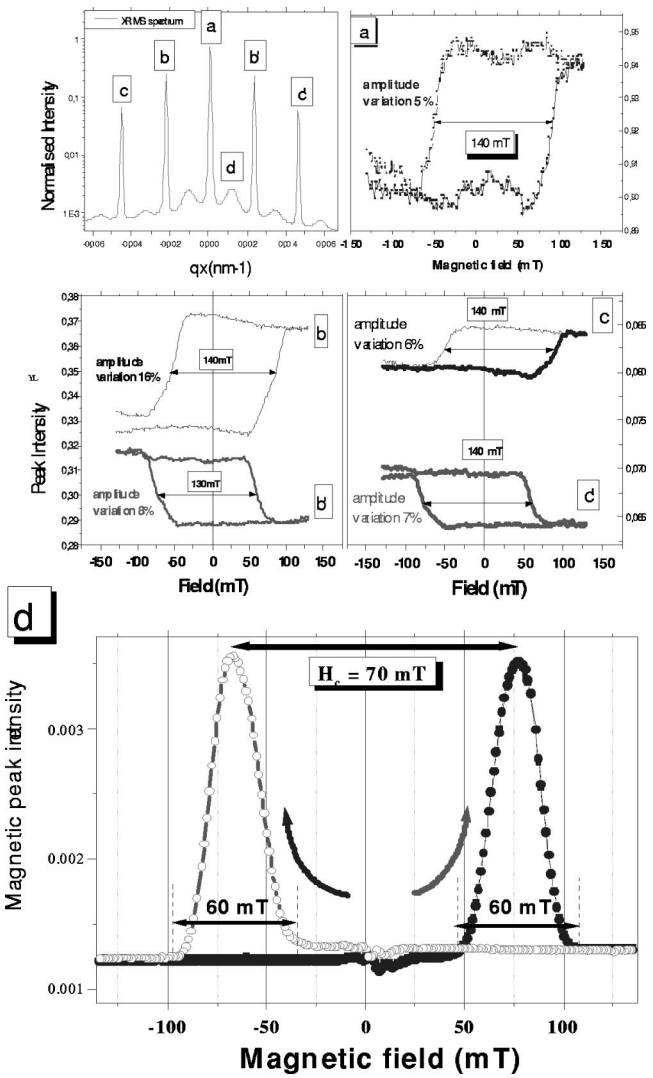

FIG. 9. Evolution of the structural peaks (a, b, b', c, and c') and, right-hand side magnetic satellite (d) intensities under *in situ* perpendicular magnetic field, describing the entire hysteresis loop, at $E=778.5$ eV (each loop is scanned with a speed of 1.15 mT/sec).

where F_S and F_M correspond to the structural and the magnetic part, respectively. One can easily see how these two parts interfere, by considering the scattered amplitude,

$$A(\mathbf{q})=\sum_n (F_S+F_M)\exp(i\mathbf{q}\cdot\mathbf{r_n})=\tilde{F}_S+\tilde{F}_M, \tag{4.2}$$

where $\tilde{F}$ denotes the Fourier transform of F.

The intensity is

$$I(\mathbf{q})=|A(\mathbf{q})|^2=|\tilde{F}_S+\tilde{F}_M|^2=|\tilde{F}_S|^2+|\tilde{F}_M|^2+2\,\mathrm{Re}(\tilde{F}_S\cdot\tilde{F}_M)$$
$$\simeq|\tilde{F}_S|^2+2\,\mathrm{Re}(\tilde{F}_S\cdot\tilde{F}_M). \tag{4.3}$$

Thus there exists an intensity component which depends on the sample magnetization. By recasting the scattering factor in a matrix form, we can clarify this expression:

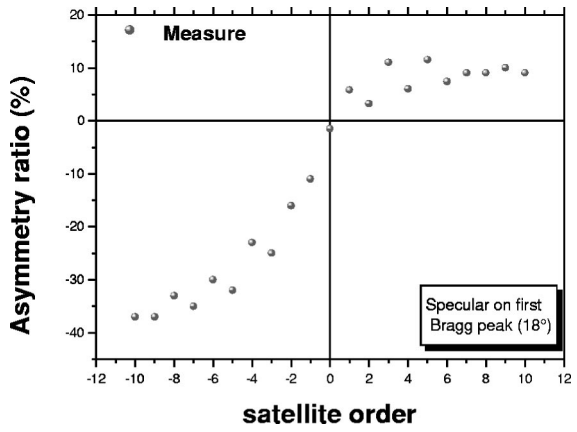

FIG. 10. Evolution of the asymmetry ratio with the order of the structural satellite at the first Bragg multilayer peak position.

$$f_n^{res}=\begin{pmatrix}1 & 0\\ 0 & \mathbf{k_i}\cdot\mathbf{k_f}\end{pmatrix}F_n^{(0)}+i\begin{pmatrix}0 & -\mathbf{k_i}\cdot\mathbf{M_n}\\ \mathbf{k_f}\cdot\mathbf{M_n} & (\mathbf{k_i}\times\mathbf{k_f})\cdot\mathbf{M_n}\end{pmatrix}F_n^{(1)}. \tag{4.4}$$

The intensity is $I=\mathrm{Tr}(\widetilde{f_n^{res}}.\rho\widetilde{f_n^{res}}^{*})$ where ρ is the density polarization matrix. In the case of circular light, and taking account that the magnetization is perpendicular to the layer we obtain

$$I=[1+(\mathbf{k_i}\cdot\mathbf{k_f})^2]\left|\sum_n F_n^{(0)}\exp(i\mathbf{q}\cdot\mathbf{r_n})\right|^2+\sum_{m,n}[\exp(i\mathbf{q}\cdot\mathbf{r}_{n,m})\times F_n^{(0)}(F_m^{(1)})^{*}+\exp(i\mathbf{q}\cdot\mathbf{r}_{m,n})F_n^{(1)}(F_m^{(0)})^{*}][\mathbf{k_i}\cdot\mathbf{M}_n+(\mathbf{k_i}\cdot\mathbf{k_f})(\mathbf{k_f}\cdot\mathbf{M}_n)]. \tag{4.5}$$

And, assuming that $F_n^{(0,1)}$ are uniforms:

$$I=[1+(\mathbf{k_i}\cdot\mathbf{k_f})^2]\left|F^{(0)}\sum_n\exp(i\mathbf{q}\cdot\mathbf{r_n})\right|^2+[\mathbf{k_i}\cdot\mathbf{M}+(\mathbf{k_i}\cdot\mathbf{k_f})\times(\mathbf{k_f}\cdot\mathbf{M})]2\,\mathrm{Re}\left(F^{(0)}(F^{(1)})^{*}\sum_n\exp(i\mathbf{q}\cdot\mathbf{r}_n)\right). \tag{4.6}$$

Thus the intensity depends linearly on the magnetization unit vector **M**. The measurements represented in Fig. 9 are performed at fixed q_x value (also fixed $\mathbf{k_i}$ and $\mathbf{k_f}$), the variable being the unit vector of magnetic profile **M**, which varies from one saturated state $\mathbf{M}_{\downarrow}=-\mathbf{z}$ to the opposite one $\mathbf{M}_{\uparrow}=+\mathbf{z}$ and induces either constructive or destructive interference, resulting in the intensities $I_{\downarrow}$ and $I_{\uparrow}$, respectively. The intensity variation detected in the specular peak (a) is directly proportional to the total magnetization and reproduces the hysteresis loop. Similar loops are also observable on all the superlattice peaks. The intensity of these peaks contains information about magnetic correlations between the lines at the grating periodicity, i.e., ferromagnetic order, which is sensitive to the hysteresis effect. One can observe a specific reversal between the left and right satellites. This dichroic effect can be quantified by an asymmetry ratio $R=(I_{\uparrow}-I_{\downarrow})/(I_{\uparrow}+I_{\downarrow})$. The evolution of the measured R ratio with the harmonic position is represented in Fig. 10.

The dependence of the quantity R with the satellite order evidences its sensitivity to the incident and outgoing angles θ_i and θ_f. Here, the measurement is performed on the first multilayer Bragg peak, so that the angles θ_i and θ_f differ slightly from the central specular position $\theta_0=18°$, the detector being at $2\theta_0=36°$.

One can see in Eq. (4.6) how the intensity I depends on the vectors $\mathbf{k}_i$ and $\mathbf{k}_f$, of defined by the angles θ_i and θ_f, thus inducing a variation of the asymmetry ratio with the satellite order. A more detailed study, based on systematic measurement, and accounting also for the asymmetry of the magnetic profile is foreseen, in order to model this result. In the present paper, we focus more on the evolution of the purely magnetic peak intensities with the magnetic field.

2. Magnetic peaks

The plot in Fig. 9, part (d), represents the variation of the intensity of the first magnetic satellite at the right-hand side, corresponding to the AF order evolution. Starting from a positive saturated state, where the whole sample is ordered ferromagnetically, the decreasing H field induces progressively the reversal of some adjacent lines and the onset of AF-ordered regions. The AF magnetic satellite intensity rises rapidly and shows a maximum at the negative coercive value $-H_c$ (complete demagnetization). For lower H values, the intensity decreases to zero (flat diffuse background) when the sample has reached the negative saturation. The same behavior is repeated symmetrically around $+H_c$ when the field describes the second part of the loop. The apparent value of the coercive field is 70 mT. This value differs slightly from the Kerr measurement (78 mT), possibly due to a different calibration. The extension of the reversal process covers a range of $\Delta H_r=60$ mT. This result is fully reproducible, regardless of the speed of the H-field sweeping. Its accuracy allows one to model the reversal of magnetization in such systems, as described below.

D. Model for the magnetization reversal process

The grating system is modeled by an assembly of N single domain lines, each carrying a magnetization $m(i)=\pm 1$ (i being the line index, varying from 1 to N). The concept of the simulation is to start with a saturated magnetic state $[m(i)=+1,\forall i]$ and to reproduce statistically the reversal processes in the magnetic grating, taking into account the magnetic dipolar coupling and the intrinsic reversal field distribution $\{B_c^i\}$ for the lines pattern.

The effective field perceived by line i is

$$B_i=B_{ext}+\sum_{j\neq j}B_d^j(i), \tag{4.7}$$

where B_{ext} is the external field value (assumed homogeneous), and $B_d^j(i)$ is the dipolar field created by the magnetic line j at the center of the line i. This field is calculated by considering the magnetic layer of each line, whose rectangular section is bc, with $b=200$ nm and $c=32$ nm,

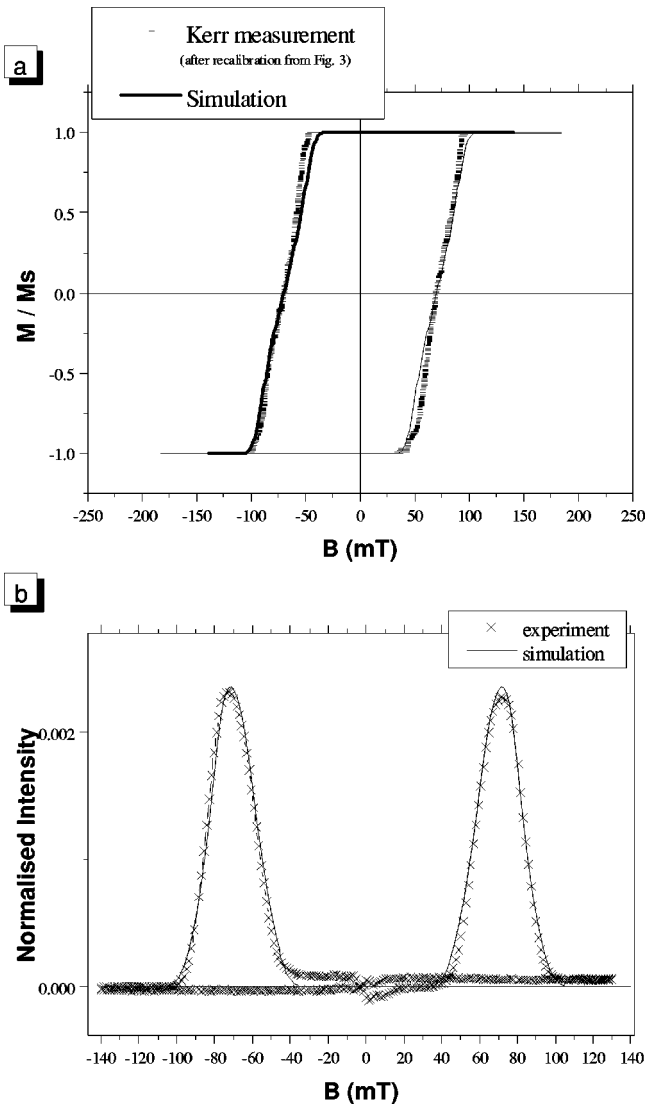

FIG. 11. Results of the simulation for $N=500$ lines and $N_s=10^4$ samplings, with $J_s=377$ mT, $B_c^0=70$ mT, and $\Delta B_c=0.09B_c^0$. (a) hysteresis loop obtained by Kerr effect, (b) AF satellite intensity evolution.

$$B_d^j(i)=-\frac{J_s}{\pi}\left[\arctan\left(\frac{2x_{ij}+b}{c}\right)-\arctan\left(\frac{2x_{ij}-b}{c}\right)\right], \tag{4.8}$$

where J_s is the saturation magnetization, multiplied by μ_0, and $x_{ij}=(j-i)p$ is the distance between the centers of the line j and the line i. In this model, the Co/Pt multilayer is considered as a single magnetic layer with a uniform mean magnetization:

$$J_S=\mu_0 M_S^{CoPt}=\mu_0 M_S^{Co}\frac{e_{Co}}{e_{tot}}, \tag{4.9}$$

e_{Co} and e_{tot} being the thickness Co and the total layer thickness, respectively 5 and 23 Å (± 1 Å), thus giving $J_s=377\pm 20$ mT. This Ising macrospin approach neglects both vertical and lateral magnetic inhomogeneities. The latter assumption is rather crude, since by evaluating the dipolar field at the center of each line, one neglects the edge effects. Nevertheless, this model provides good simulation, as we will see, and is relevant from the point of view of global magnetic ordering.

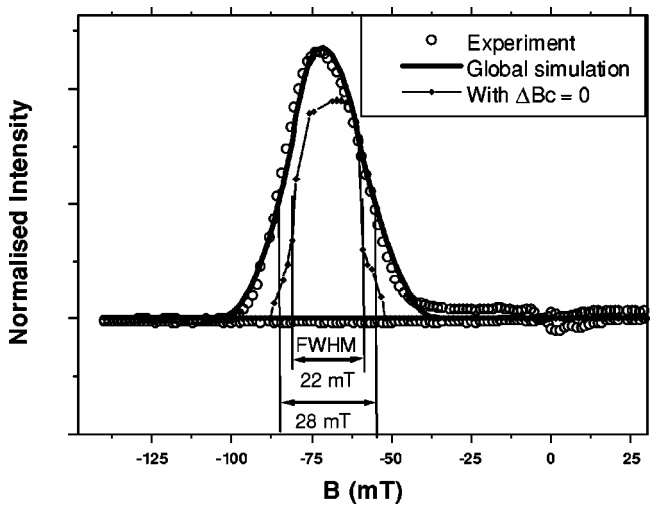

FIG. 12. Comparison between the global simulation (including $Js=377$ mT and $\Delta B_c=6.3$ mT) and a partial simulation with only dipolar coupling ($\Delta B_c=0$).

The criterion of reversal for the line i is that $|B_i|\geqslant B_c^i\geqslant 0$ (reversal from negative to positive state occurring at $+B_c^i$, and from positive to negative state occurring at $-B_c^i$). By analyzing MFM images at different stages of the reversal process, it appears that the spatial distribution $\{B_c^i\}$ arises from the structural defects, favoring domain nucleation. It will be described by a normal random distribution around a mean value B_c^0 with a variance ΔB_c.

This approach considers a step-by-step reversal of the macrospins from the initial saturated state, thus requiring us to recalculate the magnetization distribution $\{m(i)\}$ and the resulting effective-field distribution at each step. Two quantities are evaluated, respectively the total magnetization and the AF satellite intensity at $q_x=2\pi/2p$:

$$M(B_{ext})=\frac{M_S}{N}\sum_{i=1}^{N} m(i),$$

$$I(B_{ext})=\frac{I_{max}}{N^2}\left|\sum_{i=1}^{N} m(i)\exp[jq_x(ip)]\right|^2. \tag{4.10}$$

In the simulation, B_{ext} is sweeping the whole range $(-B_{sat},+B_{sat})$ with 200 steps. The parameters to be adjusted in the simulation are $(B_c^0,\Delta B_c)$ for the critical-field distribution. The position of the AF satellite (coercive field) is mainly determined by B_c^0, while the satellite size and the slope of the hysteresis loop are governed by ΔB_c and J_s.

The real sample presents about 10^4 lines of which $\sim 2\times 10^3$ are illuminated by the x rays. In the simulation, the number of lines is equal to $N=500$. Due to this limited value, the stochastic spread present in the evaluated quantities (M,I), is smoothed by taking the average over many sampling $(N_s=10^4)$. The results are represented in Fig. 11.

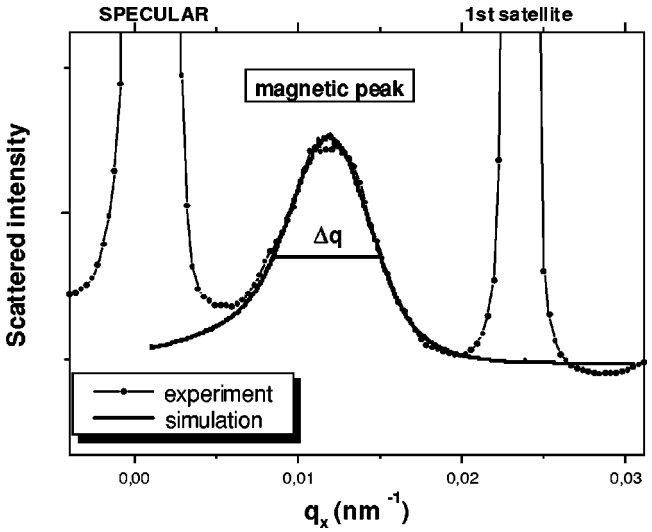

FIG. 13. Comparison between the Fourier transform of the magnetic configuration, represented in the interval of the first magnetic peak, and the experimental measure. The calculation has been done at the coercive point in the simulation ($J_s=377$ mT, $\Delta B_c=6.3$ mT, and $B_c=70$ mT).

The shape of the hysteresis loop (a) and the AF magnetic satellite evolution (b) are remarkably well reproduced. The different criteria of comparison between the experimental and the simulated curves, i.e., the position, width and shape of the magnetic satellites as well as the slope of the hysteresis loop, allows precise estimates of the parameters J_s, B_c^0, and ΔB_c.

From the modeling, with $J_s=377$ mT, we deduce the mean critical field B_c^0 to be 70 mT, and the variance $\Delta B_c=0.09B_c^0=6.3$ mT. The effective reversal field total width is $\Delta_T B=60$ mT: the reversal process, appearing at $B=40$ mT and vanishing at 100 mT, are therefore not only due to the dipolar coupling. A comparison between the dipolar contribution J_s and the defects contribution ΔB_c is shown in Fig. 12. According to a simulation with $Js=377$ mT and $\Delta B_c=0$, it appears that dipolar coupling itself generates a reversal field distribution $\Delta B_1=22$ mT FWHM, which is much smaller than the experimental value $\Delta B=28$ mT. This means that the structural defects have a significant influence on the total reversal process and stretches the reversal field extension by a quantity $\Delta B_2\simeq\Delta B-\Delta B_1=28-22=6$ mT, i.e., more than 20% of the total width. This graphically evaluated value ΔB_2 is in good agreement with the fitting of the parameter ΔB_c.

A simulation of the first magnetic satellite intensity in the Fourier space is presented in Fig. 13. This curve is obtained by calculating the Fourier transform of the magnetic configuration at the coercive point:

$$I(q)=\frac{1}{N^2}\left|\sum_j^N m_{AF}(j)\exp[iq(jp)]\right|^2, \qquad (4.11)$$

where $\{m_{AF}(j)\}$ is the magnetic configuration at $B=B_c=70$ mT, with the fitted parameters J_s and ΔB_c. At this coercive point, the line's assembly presents the largest number of AF areas. We could estimate the mean size of these AF areas: the width of the peak is $\Delta q=0.0066$ nm^{-1}, that give a magnetic correlation length about 950 nm, i.e., almost four lines. The calculation is in good agreement with the experimental result. We remind that this simulation does not take account of the charge scattering, so it does not reproduce either the specular and superlattices peaks, or the diffuse background, but only the magnetic part, which fits quite well with the experimental magnetic peak.

V. CONCLUSIONS

We have studied the magnetic order in a Co/Pt line array applying the XRMS technique to a nanostructured magnetic grating. In the chosen geometry (lines of 200-nm width separated by a 75-nm gap), the demagnetized state is dominated by an antiferromagnetic order with a mean correlation length of about four lines. The evolution of the structural and magnetic peak intensities under *in situ* magnetic field evidences the contribution of the magnetic part in the scattering factor both on the specular peak and grating satellites. This effect has been quantified by an asymmetry ratio, which presents a characteristic angular dependence. We have also followed step by step the evolution of the pure magnetic superstructure peak associated with the AF order: its intensity increases to a maximum for the highest AF order, at the coercive value evaluated to be 70 mT; this process occurs within a range of 60 mT of the H field. In order to simulate these results, we modeled the system by an assembly of macrospins assigned with a random distribution of the critical reversal field. The reversal processes are shown to be not only governed by dipolar coupling effects, but also by structural defects, which favor the domain nucleation along each line, and contribute significantly to the reversal field extension (more than 20% of the total width). This result shows the possibility to control partly the reversal processes, by modifying the deposition conditions (defect density, the structural and magnetic profile, etc.). Finally, the reproducibility of the XRMS signal evolution under field evidences the reversibility of the magnetic profile evolution, an important aspect for recording processes.

ACKNOWLEDGMENTS

We would like to thank M. D. Roper for technical help, and N. Brookes, A. Tagliaferri, and K. Larsson for their support at the ESRF ID12B beamline. We thank B. Rodmacq for providing us the samples. These experiments were performed in the framework of the PLATO program.

*Electronic address: chesnel@drfmc.ceng.cea.fr
†Electronic address: belakhovsky@cea.fr

[1] G. A. Prinz, Science **282**, 1660 (1998).
[2] P. M. Platzman and N. Tzoar, Phys. Rev. B **2**, 3556 (1970).
[3] F. de Bergevin and M. Brunel, Acta Crystallogr., Sect. A: Cryst. Phys., Diffr., Theor. Gen. Crystallogr. **A37**, 314 (1981).
[4] M. Blume, J. Appl. Phys. **57**, 3615 (1985).
[5] D. Gibbs, D. R. Harshmann, E. D. Isaacs, D. B. McWhan, D. Mills, and C. Vettier, Phys. Rev. Lett. **61**, 1241 (1988).
[6] T. Aign, P. Meyer, S. Lemerle, J.-P. Jamet, V. Mathet, C. Chappert, J. Gierak, C. Vieu, F. Rousseaux, H. Launois, and H. Bernas, Phys. Rev. Lett. **81**, 5656 (1998).
[7] S. Landis, B. Rodmacq, B. Dieny, B. Dal'Zotto, S. Tédesco, and M. Heitzmann, Appl. Phys. Lett. **75**, 2473 (1999).
[8] K. Chesnel, M. Belakhovsky, S. Landis, B. Rodmacq, G. van der Laan, E. Dudzik, S. P. Collins, and S. S. Dhesi, IEEE Trans. Magn. **37**, 1661 (2001).
[9] S. Landis, B. Rodmacq, and B. Dieny, Phys. Rev. B **62**, 12 271 (2000).
[10] J. P. Hannon, G. T. Trammell, M. Blume, and D. Gibbs, Phys. Rev. Lett. **61**, 1245 (1988).
[11] H. A. Dürr, E. Dudzik, S. S. Dhesi, J. B. Goedkoop, G. van der Laan, M. Belakhovsky, C. Mocuta, A. Marty, and Y. Samson, Science **284**, 2166 (1999).
[12] G. van der Laan, H. A. Dürr, E. Dudzik, M. D. Roper, S. P. Collins, T. P. A. Hase, and I. Pape, Synchrotron Radiat. News **12**(3), 5 (1999).
[13] M. D. Roper, G. van der Laan, H. A. Dürr, E. Dudzik, S. P. Collins, M. C. Miller, and S. P. Thompson, Nucl. Instrum. Methods Phys. Res. A **467-468**, 1101 (2001).